Proceedings of ASME Turbo Expo 2011
GT2011
June 6-10, 2011, Vancouver, British Columbia, Canada

GT2011-45404

OPTIMIZATION OF A TRANSONIC AXIAL COMPRESSOR CONSIDERING INTERACTION OF BLADE AND CASING TREATMENT TO IMPROVE OPERATING STABILITY

Jin-Hyuk Kim
Dept. of Mechanical Engineering,
Inha University
Incheon, Republic of Korea
jinhyuk@inha.edu

Kwang-Jin Choi
Dept. of Mechanical Engineering,
Inha University
Incheon, Republic of Korea
ckj97481@inha.edu

Kwang-Yong Kim
Dept. of Mechanical Engineering,
Inha University
Incheon, Republic of Korea
kykim@inha.ac.kr

ABSTRACT

A multi-objective optimization of a transonic axial compressor with circumferential casing grooves has been carried out in the present study. A hybrid multi-objective evolutionary algorithm coupled with response surface approximation is used to optimize the stall margin and design speed efficiency of the transonic axial compressor. Three-dimensional Reynolds-averaged Navier-Stokes equations with the shear stress transport turbulence model are discretized by finite volume approximations and solved on hexahedral grids for the flow analysis. The stall margin and peak adiabatic efficiency are used as objective functions for the optimization. Tip clearance and angle distribution at blade tip are considered as design variables in addition to the depth of the circumferential casing grooves which was more sensitive variable than the width in the previous work (GT2010-22396). Latin-hypercube sampling as design-of-experiments is used to generate twenty five design points within the design space. A fast non-dominated sorting genetic algorithm with an ε–constraint strategy for the local search is applied to determine the global Pareto-optimal solutions. The trade-off between two objectives is determined and discussed with respect to the representative clusters in the Pareto-optimal solutions compared to the smooth casing.

NOMENCLATURE

EFFI	Adiabatic efficiency
EXP	Experimental data
$P_{1\text{-}5}$	Control points generated from Bezier-curve
R^2	Correlation coefficient in least squares surface fitting
R^2_{adj}	Adjusted correlation coefficient

Subscript

in	Inlet
max	Maximum value
out	Outlet
ref	Reference

INTRODUCTION

Complex flow structure near the blade tip causes an axial compressor to experience instability resulting from the stall and surge at low mass flow. It is reported by Greitzer [1] that stall induces large vibratory stresses in the blade of compressors and is often unacceptable for structural reasons, and surge can lead to high blade and casing stress levels. Therefore, many researchers have numerically and experimentally investigated and analyze the flow mechanisms that result in the instability of an axial compressor [2-4].

The tip leakage vortex is known as one of the primary factors to induce the stall and surge in an axial compressor. The trajectory of the tip leakage vortex which can be affected by the geometry near the tip region, i.e., the casing treatment and the blade, has an influence on the stability of an axial compressor. To control this flow phenomenon, grooves on the casing as the passive method have been introduced to the design of an axial compressor for the last decade. Huang et al. [5] investigated the stall mechanism of the NASA Rotor 37 through the analysis of the critical flow structure near the stall. This study found that stall margin improvement can be achieved without significant penalty on the efficiency through two configurations of the circumferential grooves casing treatment (CGCT). Also, Huang et al. [6] performed a study on the effect of various configuration, width and depth of CGCT, on stall margin by numerical analysis and suggested that the stall mechanism is substantially influenced by tip clearance. Muller et al. [7] studied the effects of the number of the grooves and depth on the stall margin by three-dimensional numerical analysis. Houghton and Day [8] reported that the grooves have effects on rotor outflow blockage, and the near casing flow field was then studied using both experimental and computational methods. Rabe and Hah [9] investigated the fundamental flow mechanism by the circumferential grooves on the casing of a transonic compressor.

Many other methods to enhance the stability and the stall margin have been applied to axial compressors as well as CGCT. Wilke and Kau [10] reported the impact of axial slots on the flow field in a transonic rotor blade row. Unsteady flow simulations in an axial compressor with four different semicircular slots were performed with a three-dimensional time accurate Favre-averaged Navier-Stokes flow solver by Hembera et al. [11]. Jian and Hu [12] conducted numerical investigation of the effect of inlet distortion on an axial compressor with CGCT.

Recently, many engineering designs involve multiple disciplines and simultaneous optimization of multiple objectives related to each discipline. These design problems, usually known as multi-objective problems, require simultaneous consideration of all objectives to optimize the system. The fast and elitist non-dominated sorting genetic algorithm (NSGA-II) by Deb [13] generates the Pareto-optimal solutions (POSs) using an evolutionary algorithm. Lotfi et al. [14] performed an optimization of a low speed fan cascade using a genetic algorithm. They selected the thickness distribution and the camber line as design variables. Kim et al. [15] conducted a hybrid multi-objective evolutionary algorithm (MOEA) of a centrifugal compressor impeller with four design variables that defined the impeller hub and shroud contours in meridian terms. Lastly, Samad and Kim [16] reviewed the performance of various surrogate models applied to multi- and single-objective design optimizations of a transonic axial compressor.

In this study, a hybrid MOEA [17] coupled with response surface approximation (RSA) [18] was performed to optimize the stall margin and efficiency of a transonic axial compressor. In the previous work [19], the circumferential casing grooves were optimized using two design variables, i.e., the depth and the width of the circumferential casing grooves. However, the present study was extended to three design variables including the variables related to blade shape, i.e., tip clearance and angle distribution at blade tip in addition to the depth of the circumferential casing grooves which was more sensitive variable than the width in the previous work [19]. Thus, the present multi-objective optimization is effectively used for the design of a transonic axial compressor with casing grooves considering the interaction of blade and casing grooves, and it is expected for designers to meet their design requirements with regard to the stall margin and peak adiabatic efficiency from the POSs obtained in this work.

AXIAL COMPRESSOR MODEL

An axial compressor with NASA Rotor 37 was considered in this study for the multi-objective optimization to improve the operating stability. NASA Rotor 37 is well known rotor for the experimental data by Reid and Moore [20].

The rotor operates at a speed of 17188.7 rpm, and total pressure ratio and adiabatic efficiency are 2.106 and 88.9% at 20.19 kg/s, respectively. The blade sections of NASA rotor 37 are defined by multiple-circular-arc (MCA). Tip clearance is 0.356 mm (0.47% span), chocking mass flow is 20.93 kg/s, and near stall point is 0.925 of the choke flow. The detailed specifications of NASA rotor 37 are listed in Table 1.

COMPUTATIONAL METHODS

The commercial CFD code ANSYS-CFX 11.0 [21] was used for the flow analysis. Blade profile creation, computational mesh generation, boundary condition definitions, flow analysis and post processing were performed by Blade-Gen, Turbo-Grid, CFX-Pre, CFX-Solver, and CFX-Post, respectively. And, in order to define the circumferential casing grooves, groove creation and mesh generation were performed by Design-Modeler and ICEM-CFD, respectively.

Three-dimensional steady RANS analysis based for the compressor with the circumferential casing grooves has been performed for the present optimization since it is possible to assume that the flow is steady in the operating range. In this study, the computation for determination of the operating range was carried out from the chocking mass flow up to the final converged point by reducing mass flow rate. A single blade-to-blade passage in the compressor is selected as the computational domain in order to save computation time. This simplification of the domain is based on the assumption that the flow between two adjacent blades is periodic about rotational direction.

The numerical stall inception point could be identified from the last converged point by reducing the normalized mass flow rate by 0.002. The convergence criterion was suggested by Chen et al. [22] as follows:

1. The inlet mass flow rate variation is less than 0.001kg/s for 300 steps.
2. The difference between inlet and outlet mass flow rate is less than 0.5%.
3. At that time the adiabatic efficiency variation is less than 0.03% per 100 steps.

The same convergence criterion was used to find the numerical stall inception point in this work.

Table 1 Design specifications of the axial compressor with NASA Rotor 37

Design mass flow rate, kg/s	20.19
Rotational speed, rpm	17188.7
Total pressure ratio	2.106
Inlet hub-tip ratio	0.7
Blade aspect ratio	1.19
Tip relative inlet Mach number	1.48
Hub relative inlet Mach number	1.13
Tip solidity	1.29
Number of rotor blade	36

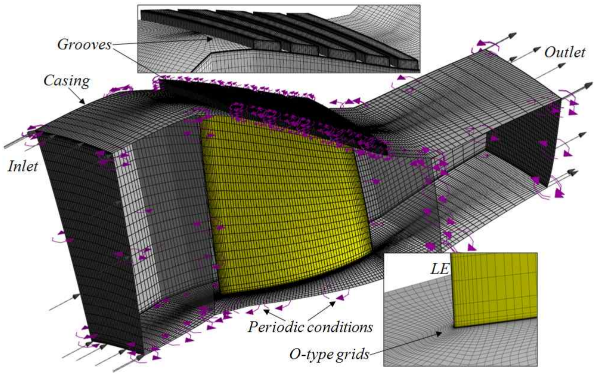

Fig. 1 Boundary conditions and hexahedral grid system in the computational domain

Fig. 1 shows the boundary conditions of the computational domain for the numerical analysis. The groove domains with single blade-to-blade passage are modeled as rotating domain. However, the groove walls are set as the stationary with the count rotating wall condition. Ideal gas was used as the working fluid. Total pressure and total temperature at the inlet were set to 101,325 Pa and 288.15 K, respectively. Mass flow rate was set at the outlet. Adiabatic walls with no slip and hydraulically smooth conditions were considered at the solid boundaries. The general grid interface (GGI) method was used for the connection between the passage and the grooves. The GGI method is used when the grids on either side of two connected surfaces do not match [21].

Three-dimensional RANS equations with the shear stress transport (SST) turbulence model [23] were discretized using finite volume approximations. A high-resolution scheme which is second-order accurate in space was used to solve the convection-diffusion equations. The SST model uses a k-ω model in the near-wall region, a k-ε model in the bulk domain, and a blending function to ensure a smooth transition between two models. In this study, the near wall grid resolution was adjusted to keep $y^+<2$ to implement the low-Reynolds number version of the SST model.

A structured grid system with O-type grids near the blade surfaces and H/J/C/L grids in other regions was constructed in the computational domain. The optimum grid system selected by the grid-independency test has 480,000 nodes except for the grooves as reported by the previous work [19]. In the optimum grid system, the tip clearance is constructed with 62,160 nodes. And, five grooves are constructed with 140,000 nodes. Fig. 1 shows the typical example of a hexahedral grid system used for the numerical analysis.

The computations were performed by an Intel Core I7 CPU, 2.67 GHz PC. The computational time was approximately 6-7 hours.

OPTIMIZATION METHODOLOGY

The overall optimization procedure is described in the flow chart shown in Fig. 2. Each step in this procedure is explained in the following sections in detail.

Objective Functions

The objectives of the present optimization are to maximize both the stall margin (*SM*) and peak adiabatic efficiency (η_{peak}), which were selected as objective functions for the shape optimization of the blade and the circumferential casing grooves. These objective functions are defined as follows:

$$SM = \left(\frac{m_{peak}}{m_{stall}} \times \frac{PR_{stall}}{PR_{peak}} - 1 \right) \times 100\% \tag{1}$$

$$\eta_{peak} = \frac{\left(\frac{P_{t,out}}{P_{t,in}}\right)^{\frac{\gamma-1}{\gamma}} - 1}{\left(\frac{T_{t,out}}{T_{t,in}}\right) - 1} \tag{2}$$

where, m and PR indicate the mass flow rate and total pressure ratio, respectively, and the subscripts *peak* and *stall* refer to the peak adiabatic efficiency point and the near stall point, respectively. γ, P_t, and T_t indicate the specific heat ratio, total pressure, and total temperature, respectively.

Design Variables

The operating range of NASA Rotor 37 is limited by the occurrence of stall phenomena at low mass flow rate. However, it is possible to postpone and suppress the stall phenomena by modifying the geometry near the blade tip region with installation of the circumferential casing grooves.

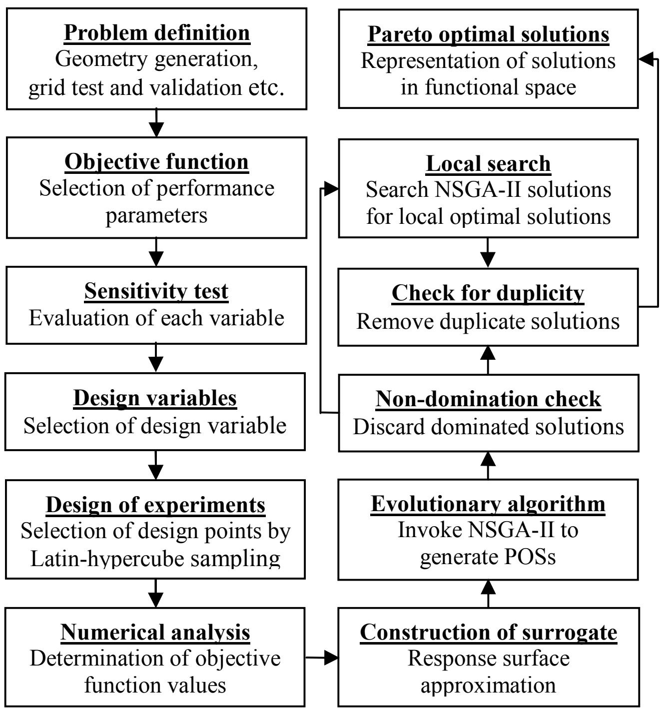

Fig. 2 Optimization procedure

In the previous work [19] to suppress the stall phenomena, the circumferential casing grooves were optimized using two design variables, the depth and the width of the circumferential casing grooves.. However, the present study employs three design variables including the tip clearance (T) and the angle (β) distribution at blade tip in addition to the depth (D) of the circumferential casing grooves.

Fig. 3(a) shows the definitions of the variables, T and D. The five circumferential casing grooves are evenly installed from the leading edge (LE) to the trailing edge (TE). The width of each groove is 16% tip axial chord and the gap is 5% tip axial chord of NASA rotor 37.

The angle, β is defined as an angle between the axis of rotation and a tangent of the camber line. β distribution at blade tip is illustrated in Fig. 3(b). In the present study, β distribution is changed on blade tip of the fixed meridional geometry by the control points represented by the fourth-order Bezier-curve [24] as shown in Fig. 3(b). The advantage of using the Bezier-curve for shape parameterization is that only control points located along the curves can control the curves. When one control point in the Bezier-curve is moved vertically, the others are being kept fixed. Thus, each control point is controlled independently, and these all points can be considered as design variables. In the present study, to limit the number of design variables, all control points are being kept except for the control point P_3. Fig. 3(c) shows an example of a changed blade shape with the variation of β distribution at blade tip.

To conduct the design optimization, it is important to find the feasible and practical design space that is formed by the ranges of the design variables. The range of each design variable is decided through sensitivity test as shown in Table 2.

Latin-Hypercube Sampling (LHS)

Design points within the design space were selected with the help of Latin-hypercube sampling (LHS) [25] as design-of-experiment (DOE). LHS, an effective sampling method in the design and analysis of computer experiments (DACE) [26], is a matrix of order $m \times n$, where m is the number of levels to be examined and n is the number of design variables. Each of n columns of the matrix containing levels 1, 2, … , m is randomly paired to form the LHS. LHS generates random sample points, ensuring that all portions of the design space are represented. In this study, LHS was used as a design-of-experiment to generate twenty five design points within the design space.

Response Surface Approximation (RSA)

In the present study, RSA [18] is employed as a surrogate model, and applied for predicting the objective function values in the design space. RSA is a methodology of fitting a polynomial function for discrete responses obtained from numerical calculations. It represents the association between design variables and response functions. The constructed response of a second-order polynomial RSA can be expressed as follows:

Table 2 Ranges of the design variables

Variables	Lower bound	Upper bound
D, (mm)	0.214	0.641
β, (deg)	60.04	69.62
T, (mm)	0.178	0.534

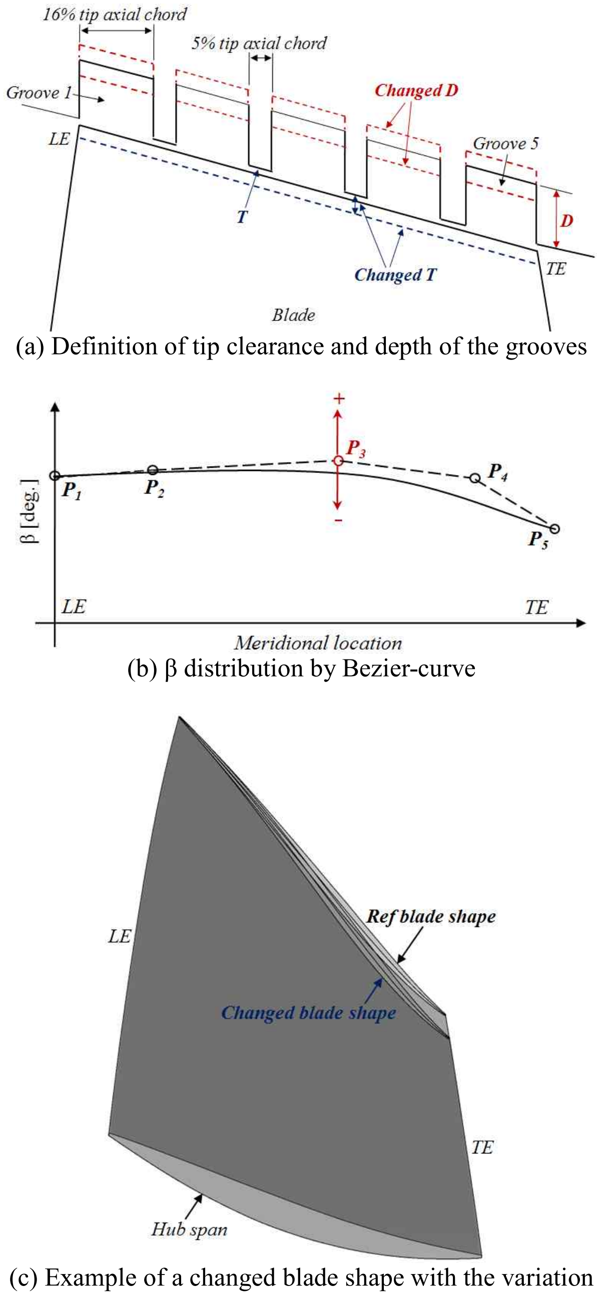

(a) Definition of tip clearance and depth of the grooves

(b) β distribution by Bezier-curve

(c) Example of a changed blade shape with the variation of β distribution at blade tip

Fig. 3 Definition of design variables

$$f(x) = C_0 + \sum_{j=1}^{N} C_j x_j + \sum_{j=1}^{N} C_{jj} x_j^2 + \sum_{i \neq j} \sum C_{ij} x_i x_j \qquad (3)$$

where, C, N, and x indicate the regression analysis coefficients, the number of design variables, and a set of design variables, respectively, and the number of regression analysis coefficients (C_0, C_i, etc.) is $(N+1)\times(N+2)/2$.

Hybrid Multi-Objective Evolutionary Algorithm (MOEA)

In this study, a hybrid MOEA [17] was used to obtain the global POSs for the multi-objective optimization problem. In this method, first, approximate POSs were obtained for two objective functions using real coded NSGA-II [13]. Here, real coded means that the crossover and mutations were conducted in real space to obtain a response of NSGA-II. These solutions were then refined by searching a local optimal solution for each objective function over all NSGA-II-obtained optimal solutions using sequential quadratic programming (SQP) [27] with NSGA-II solutions as initial guesses.

In the present study, the first objective is optimized, whereas the second objective is fixed, and the local search is repeated for the second objective by keeping the first objective as a fixed value. This process produces two new sets of optimal solutions, which are then merged with the NSGA-II solutions. From these solutions, dominated solutions are discarded, and then duplicate solutions are removed to produce the global POSs. Subsequently, the process of local search is conducted to improve the quality of the POSs.

To find representative solutions from the global POSs, these POSs were grouped into user-defined clusters by applying *K*-means clustering [26]. It is an iterative alternating fitting process to form the number of specified clusters. These clusters are distributed along the POSs.

RESULTS AND DISCUSSION

Validation

In order to evaluate the accuracy of the numerical analysis, results of the flow analysis were validated in comparison with the experimental data prior to the design optimization. The compressor used for this validation was regarded as the reference shape, which has the smooth casing without the circumferential casing grooves. Fig. 4 shows results of the validation conducted in the previous work [19] via comparison of the performance curves for the total pressure ratio and isentropic efficiency between the experimental data [28] and the results of RANS analyses. As shown in Fig. 4, the numerical results show some uniform underestimations of the total pressure ratio and isentropic efficiency through whole mass flow range, but they have good agreements with the experimental test data in terms of the tends. It was found by the experiment that the near stall point is 0.925 which is the mass flow normalized by the chocking mass flow, while the near stall point of the numerical result based on the convergence criterion is 0.921.

Results of the Multi-Objective Optimization

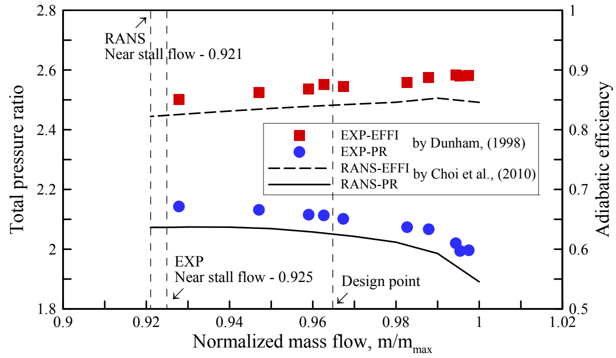

Fig. 4 Validation of the flow analysis [19]

Table 3 Results of ANOVA and regression analysis

Objective functions	R^2	R^2_{adj}	RMSE	CV errors
SM	0.958	0.949	3.90×10^{-2}	8.45×10^{-2}
η_{peak}	0.983	0.945	4.28×10^{-2}	5.62×10^{-4}

In the present study, RSA models were constructed for both objective functions, the stall margin and peak adiabatic efficiency, by using the results of RANS analysis at twenty five design points selected by LHS. For the RSA models, an analysis of variance (ANOVA) and a regression analysis replete with t-statistics [18] were performed to measure the uncertainty in the set of coefficients in the polynomial. The values of R^2 and R^2_{adj} for the second-order curve-fitting and the root mean square error (RMSE) for the RSA model are listed in Table 3. The values of R^2_{adj} for both objective functions, the stall margin and peak adiabatic efficiency, are 0.949 and 0.945, respectively. These values are reliable according to the $0.9 < R^2_{adj} < 1.0$ range suggested by Ginuta [29] for accurate prediction of RSA model. Leave-one-out cross-validation (CV) [30] was also performed to assess the accuracy of the RSA model. Although it is uncertain how well the CV is correlated with accuracy of the RSA model, the estimation of the generalization errors is nearly unbiased, as it takes into account the CV of the RSA model at every design point. The estimations of the CV errors are shown in Table 3.

A hybrid MOEA based on the constructed response by the RSA model was used to obtain the global POSs through the real-coded NSGA-II, which are invoked for obtaining well-spread approximate POSs with 250 generations and 100 populations, and the crossover and mutation probabilities are decided as 0.95 and 0.25, respectively. And, the crossover and mutation parameters are set to 10 and 50, respectively. Here, these parameters were adjusted one-by-one to suit the nature of the problem.

Fig. 5 represents the global POSs with the representative clusters A and B, and the objective function values at design points. Since both objective functions, the stall margin and peak adiabatic efficiency, were maximized, the POSs resemble a convex front. For every fixed value of one objective function, there is one optimal value for the other objective function. Each extreme end of the POSs represents a pair of the highest value of the one objective function and the lowest value of the other objective function. Since the objective functions are conflicting in nature, the improvement of one objective function leads to the decline of the other. No solution out of these POSs is superior to any other one with respect to both objectives since each solution is a global POS.

The trade-off analysis shows that the higher peak adiabatic efficiency can be obtained at the cost of the lower stall margin and vice versa. Two representative clusters A and B in the global POSs were selected through *K*-means clustering as shown in Fig. 5 and Table 4. These clusters were reproduced through RANS analysis and compared with the smooth casing in Table 4. In Fig. 5, the cluster A represents high peak adiabatic efficiency with low stall margin. On the other hand, the cluster B represents low peak adiabatic efficiency with high stall margin.

Values of the design variables corresponding to the clusters in the POSs are shown in Table 4. An increasing trend is shown for the design variable, *D* to have more extended stall margin. The clusters A and B show increases in stall margin of 2.419% and 5.316%, respectively, however, slightly decreases in peak adiabatic efficiency by 0.028% and 0.146%, respectively, compared to the smooth casing. Consequently, the clusters show much extended stall margins and slightly lower peak adiabatic efficiencies.

Performance Characteristics

Fig. 6 indicates the performance characteristics of the smooth casing, clusters A and B for the total pressure ratio and the adiabatic efficiency. As shown in Fig. 6(a), the near stall point of smooth casing, clusters A and B were predicted to be 0.921, 0.905 and 0.882, respectively. And total pressure ratios at near stall point are 2.073, 2.074 and 2.068, respectively. Fig. 6(b) shows that the peak adiabatic efficiencies of the smooth casing, clusters A and B are 85.122%, 85.094% and 84.976%, respectively. These results show that cluster A has higher peak adiabatic efficiency than cluster B has higher stall margin. From these results, it is found that the application of the circumferential casing grooves contributes to the decrease in the stall mass flow resulting in the improvement of the stall margin while resulting in slightly decrease in the peak adiabatic efficiency as reported by many researchers [8, 11 and 12].

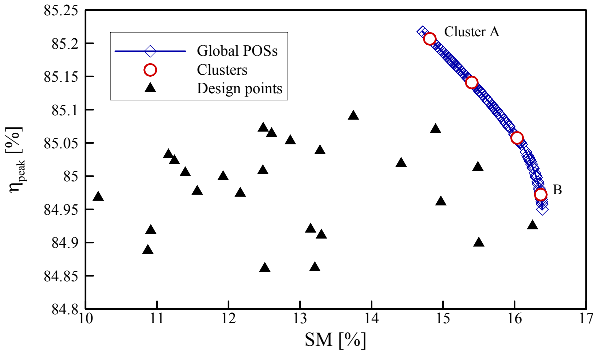

Fig. 5 POSs by hybrid MOEA and design points by LHS

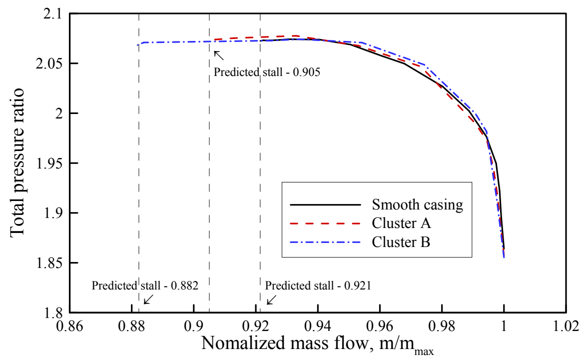

(a) Total pressure ratio

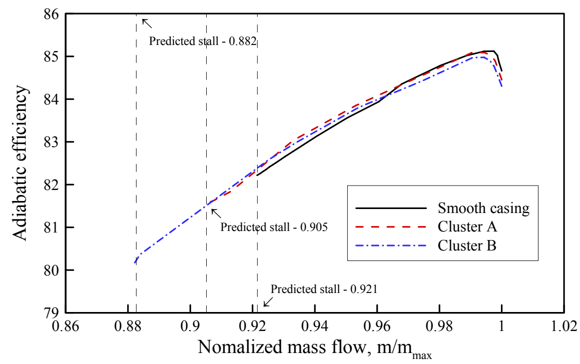

(b) Adiabatic efficiency

Fig. 6 Performance Characteristics

Table 4 Design variables and objective function values for two typical POSs

Designs	Design variables			MOEA prediction		RANS		Increment	
	D, (mm)	β, (deg.)	*T*, (mm)	*SM*, (%)	η_{peak}, (%)	*SM*, (%)	η_{peak}, (%)	*SM*, (%)	η_{peak}, (%)
Smooth casing	-	64.62	0.356	-	-	11.633	85.122	-	-
Cluster A	0.221	69.20	0.178	14.815	85.206	14.052	85.094	2.419	-0.028
Cluster B	0.427	68.41	0.193	16.367	84.972	16.949	84.976	5.316	-0.146

Analyses of Internal Flow Fields

In order to find the main factors responsible for the improvement of the performance of the axial compressor with the circumferential casing grooves, the internal flow fields of the representative clusters A and B were compared with the smooth casing in Figs. 7-9.

Fig. 7 shows the trajectories of the tip leakage vortices at near stall point of the smooth casing ($m/m_{max} = 0.921$) for the smooth casing, clusters A and B. The tip leakage vortex is produced at LE near blade tip by the interaction of the tip leakage flow and the incoming flow. In the axial compressor without the circumferential casing grooves, the tip leakage vortex is mainly driven by the tip leakage flow, and proceeds along the pressure surface of the blade, as shown in Fig. 7(a). On the other hand, the pressure gradient over the blade tip is reduced with the installation of the circumferential casing grooves. Hence, Figs. 7(b) and (c) show that the trajectory of the tip leakage vortex is mainly driven by the incoming flow, resulting in the trajectory of the tip leakage vortex close to the passage center. Also, the decrease in the pressure gradient reduces the velocity of the tip leakage vortex. The broader tip clearance and the deeper circumferential casing grooves induce the decrease in the pressure gradient over the blade tip region, which results in a decrease in the velocity of the tip leakage vortex. Thus, the cluster B shows that the trajectory of the tip leakage vortex becomes closer to the passage center since it is mainly driven by the incoming flow due to the decrease in the velocity of the tip leakage vortex compared to the cluster A as shown in Figs. 7(b) and (c).

The static pressure distributions on blade-to-blade surface at 98% span at near stall point for the smooth casing, clusters A and B are shown in Fig. 8. Fig. 8(a) shows that the blade tip stall is observed near LE of the suction surface in case of the smooth casing resulted from the high pressure occurred near LE by the deceleration of the inflow. These results were also demonstrated by Wilke et al. [31]. They reported that the inflow's angle of attack is very steep especially near the blade tip. The inflow cannot completely follow the direction given by the blade profile. The consequences are an extended separation zone at the blade suction side and a significant deceleration of the inflow at the upstream part of the following pressure side. Meanwhile, in clusters A and B, the postponed blade tip stalls are shown near LE of the suction surface with the grooves. Especially, cluster B shows the suppressed blade tip stall. It is thought that the incoming flow can follow the direction of the blade profile since the pressure near LE of the pressure surface is decreased by the variation of the angle of attack with the optimized angle distribution at blade tip and grooves.

Fig. 9 shows the static pressure distributions on the pressure and suction surfaces of the blade at 98% span for the smooth casing, clusters A and B. With the circumferential casing grooves, the change in the pressure difference between the pressure and suction surfaces is observed at each groove location. It is thought that a remarkable reduction in pressure difference occurs near the LE region due to a decrease in blade loading near the LE by the variation of the angle of attack, while the pressure difference at the location of the third groove is increased.

Fig. 10 shows the static entropy contours for the smooth casing, clusters A and B on a meridional plane at each peak efficiency point. The values are averaged in circumferential direction. As shown in Fig. 10, the application of the circumferential casing grooves had negative effects on the efficiency of an axial compressor. Higher entropy generation is observed near the casing of the axial compressor with the circumferential casing grooves compared to the smooth casing. This explains the inevitable decrease in the efficiency of the compressor. However, as shown in Figs. 10(b) and (c), entropy generation of the cluster A near the casing was significantly reduced compared to the cluster B. This reduction in entropy generation contributes to the recovery of the efficiency.

Fig. 11 shows the tangential velocity contours in openings of the circumferential casing grooves for the clusters A and B at each peak efficiency point. The application of the circumferential casing grooves results in a tip leakage vortex closer to the passage center that generates more losses near the tip region. However, as shown in Fig. 11, the cluster A shows slightly higher tangential velocity in openings of the circumferential casing grooves compared to the cluster B. The higher velocity makes the tip leakage flow closer to the pressure surface of the blade, and consequently reduces the losses by the tip leakage vortex near the tip region.

CONCLUSION

Optimization of a transonic axial compressor with a hybrid MOEA coupled with RSA model was performed to improve the performance of the compressor with circumferential casing grooves considering the interaction of blade and the casing treatment. In order to optimize the stall margin and peak adiabatic efficiency of the compressor with the circumferential casing grooves, the depth of the circumferential casing grooves, angle distribution at blade tip, and tip clearance were selected as the design variables. The flow fields of the smooth casing, the representative clusters A and B in the POSs were analyzed to find the changes through the optimization. Comparison among the smooth casing, the clusters A and B showed that improvement in the stall margin and a slight deterioration in the peak adiabatic efficiency result from the introduction of the grooves. The extension of the stall margin is attributed to suppression of the blade tip stall on the suction surface near LE by the variation of the angle of attack, and the reduction in peak adiabatic efficiency is minimized by the application of the circumferential casing grooves. The present multi-objective optimization can be effectively used for the design of a transonic axial compressor with the circumferential casing grooves, and it is expected for designers to meet their design requirements with regard to the stall margin and peak adiabatic efficiency from the global POSs.

ACKNOWLEDGMENTS

This research was supported by the Korea Institute of Industrial Technology Evaluation and Planning (ITEP) grant

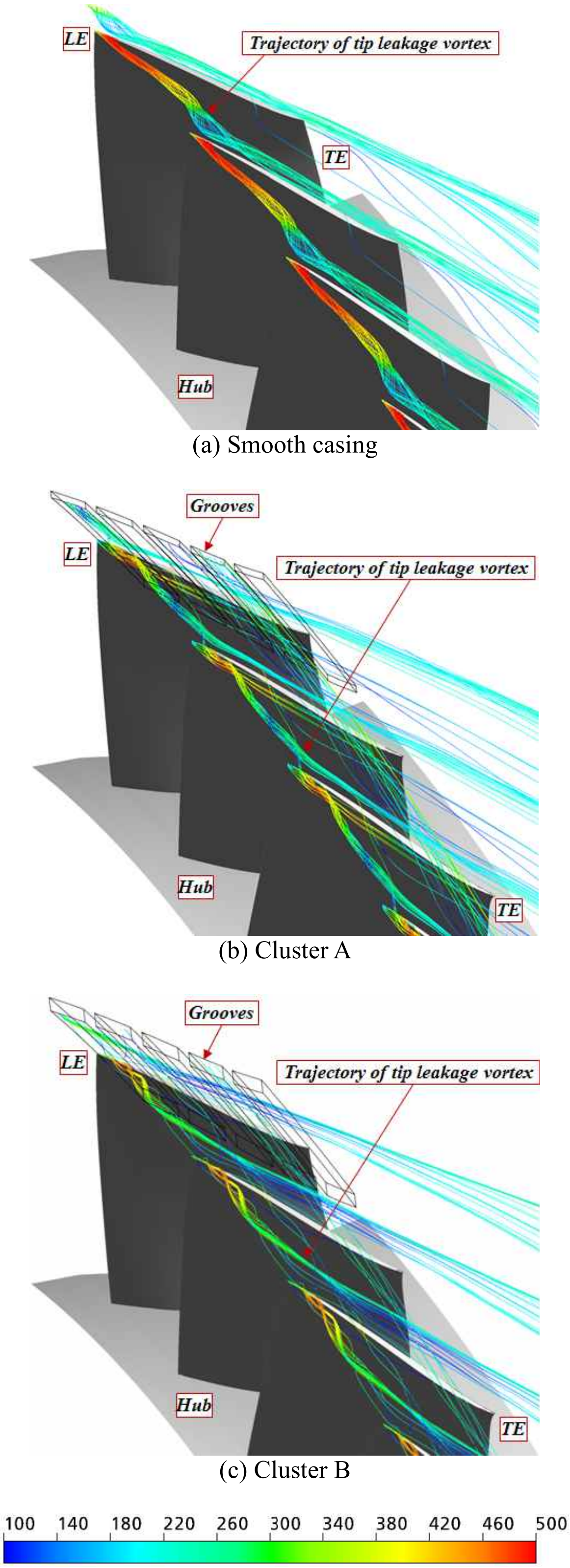

Fig. 7 Trajectory of the tip leakage vortex at near stall point of the smooth casing, m/m_{max} = 0.921 (unit: m/s)

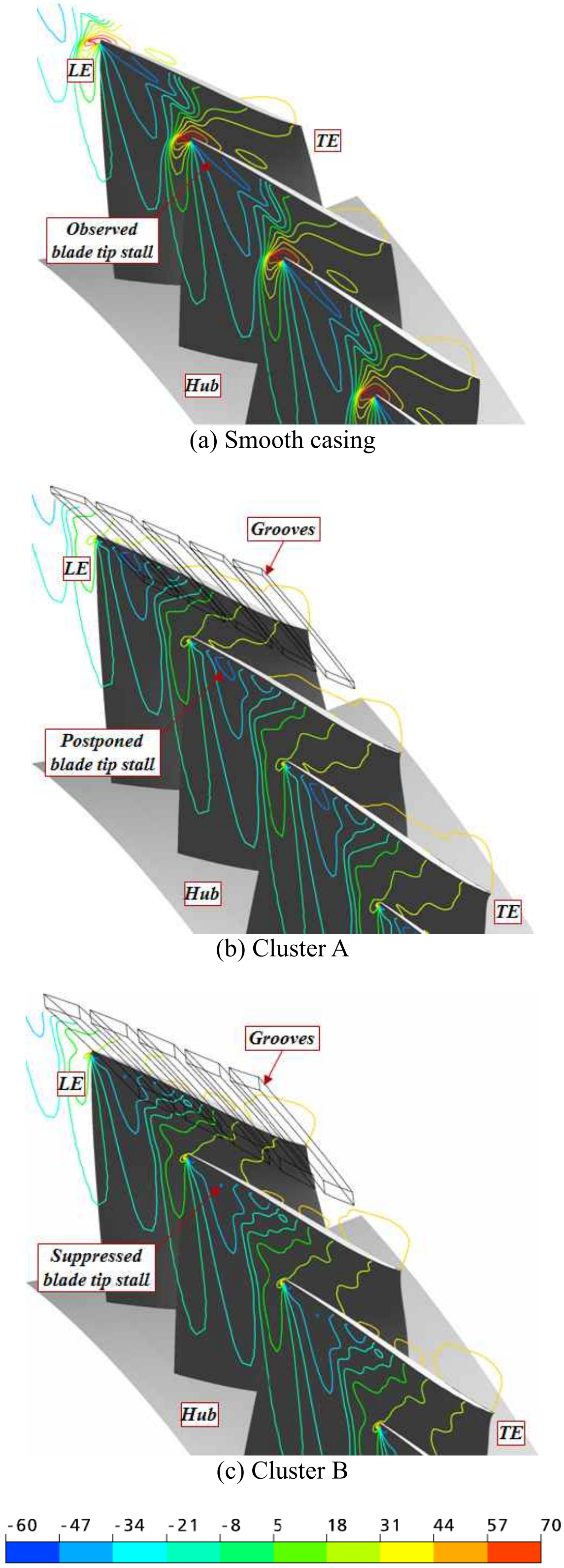

Fig. 8 Static pressure distributions on 98% span at near stall point of the smooth casing, m/m_{max} = 0.921 (unit: kPa)

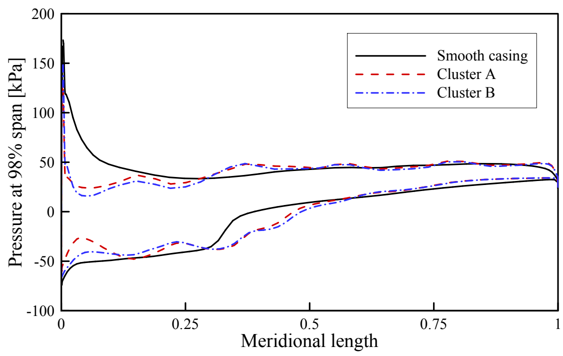

Fig. 9 Static pressure distribution at near stall point of the smooth casing, m/m_{max} = 0.921 (98% span)

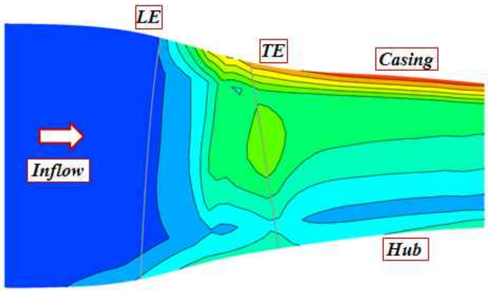

(a) Smooth casing

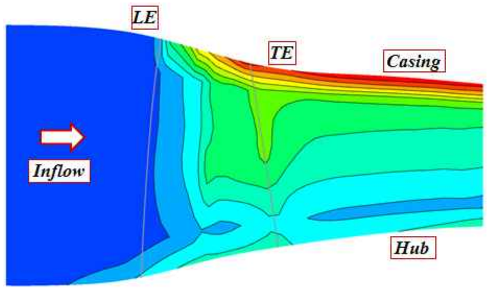

(b) Cluster A

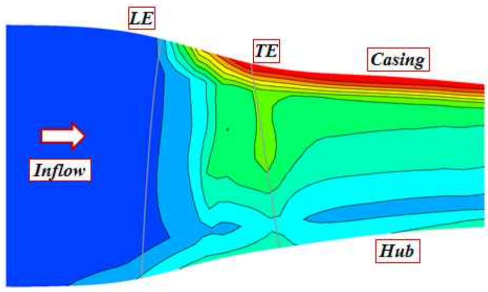

(c) Cluster B

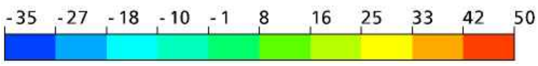

Fig. 10 Static entropy contours on a meridional plane at each peak adiabatic efficiency point (unit: J/kg·K)

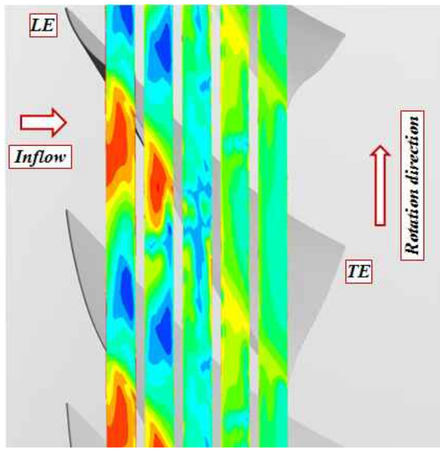

(a) Cluster A

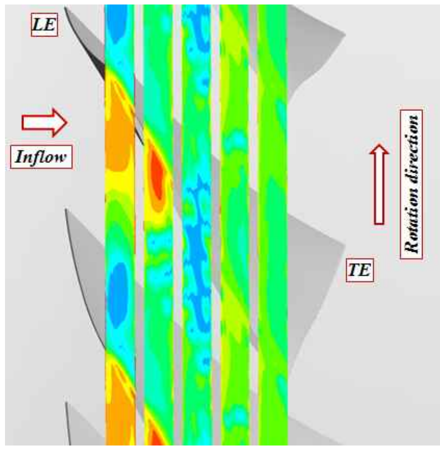

(b) Cluster B

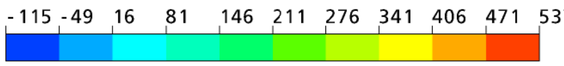

Fig. 11 Tangential velocity contours in opening of the grooves at peak efficiency point (unit: m/s)

funded by the Ministry of Knowledge Economy (No. 10031771).

REFERENCES

[1] Greitzer, E. M., 1980, "Review-Axial Compressor Stall Phenomena," ASME Journal of Fluids Engineering, Vol. 102, No.2, pp. 132-151.

[2] Choi, M. S., Oh, S. H., Ko, H. Y., and Baek, J. H., 2008, "Effects of the Inlet Boundary Layer Thickness on Rotating Stall in an Axial Compressor," ASME Turbo Expo 2008, Berlin, Germany, GT2008-50886.

[3] Saxer-Felici H. M., Saxer, A. P., Inderbitzin, A., and Gyarmathy, G., 2000, "Numerical and Experimental Study of Rotating Stall in an Axial Compressor Stage," AIAA Journal, Vol. 38, No. 7, pp. 1132-1141.

[4] Gourdain, N., Burguburu, S., Leboeuf, F., and Miton, H., 2006, "Numerical Simulation of Rotating Stall in a Subsonic Compressor," Aerospace Science and Technology, Vol. 10, No. 1, pp. 9-18.

[5] Huang, X. D., Chen, H. X., Shi, K., and Fu, S., 2010, "An Analysis of the Circumferential Grooves Casing Treatment for Transonic Compressor Flow," Science china-Physics, Mechanics & Astronomy, Vol. 53, No. 2, pp. 353-359.

[6] Huang, X. D., Chen, H., and Fu, S., 2008, "CFD Investigation on the Circumferential Grooves Casing Treatment of Transonic Compressor," ASME Turbo Expo 2008, Berlin, Germany, GT2008-51107.

[7] Muller, M. W., Schiffer, H. P., and Hah, C., 2007, "Effect of Circumferential Grooves on the Aerodynamic Performance of an Axial Single-stage Transonic Compressor," ASME Turbo Expo 2007, Montreal, Canada, GT2007-27365.

[8] Houghton, T., and Day, I., 2009, "Enhancing the Stability of Subsonic Compressor Using Casing Grooves," ASME Turbo Expo 2009, Orlando, USA, GT2009-59210.

[9] Rabe, D. C., and Hah, C., 2002, "Application of Casing Circumferential Grooves for Improved Stall Margin in a Transonic Axial Compressor," ASME Turbo Expo 2002, Amsterdam, Netherlands, GT2002-30641.

[10] Wilke, I., and Kau, H. P., 2004, "A Numerical Investigation of the Flow Mechanisms in a High Pressure Compressor Front Stage with Axial Slots," ASME Journal of Turbomachinery, Vol. 126, No. 3, pp. 339-349.

[11] Hembera, M., Kau, H. P., and Johann, E., 2008, "Simulation of Casing Treatments of a Transonic compressor stage," International Journal of Rotating Machinery, Vol. 2008, Article ID 657202.

[12] Jian, H., and Hu, W., 2008, "Numerical Investigation of Inlet Distortion on an Axial Flow Compressor Rotor with Circumferential Groove Casing Treatment," Chinese Journal of Aeronautics," Vol. 21, No. 8, pp. 496-505.

[13] Deb, K., 2001, Multi-objective optimization using evolutionary algorithms, 1st ed., John Wiley & Sons Inc., Chichester, England.

[14] Lotfi, O., Teixeira, J. A., Ivey, P. C., Sheard, G., and Kinghorn, I. R., 2005, "Aerodynamic Optimization of Industrial Fan Blade Cascades," ASME Turbo Expo 2005, Nevada, USA, GT2005-68385.

[15] Kim, J. H., Choi, J. H., Husain, A., and Kim, K. Y., 2010, "Multi-Objective Optimization of a Centrifugal Compressor Impeller through Evolutionary Algorithms," Proceedings of the Institution of Mechanical Engineers, Part A-Journal of Power and Energy, Vol. 224, No. 5, pp. 711-721.

[16] Samad, A., and Kim, K. Y., 2009, "Surrogate Based Optimization Techniques for Aerodynamic Design of Turbomachinery," International Journal of Fluid Machinery and Systems, Vol. 2, No. 2, pp. 179-188.

[17] Deb, K., and Goel, T., 2001, "A Hybrid Multi-Objective Evolutionary Approach to Engineering Shape Design," Proceedings of evolutionary multi-criterion optimization conference, Zurich, Switzerland, pp. 385-399.

[18] Myers, R. H., and Montgomery, D. C., 1995, Response surface methodology: process and product optimization using designed experiments, John Wiley & Sons, New York, USA.

[19] Choi, K. J., Kim, J. H., and Kim, K. Y., 2010, "Design Optimization of Circumferential Casing Grooves for a Transonic Axial Compressor to Enhance Stall Margin," ASME Turbo Expo 2010, Glasgow, UK, GT2010-22396.

[20] Reid, L., and Moore, R. D., 1978, "Design and Overall Performance of Four Highly-Loaded, High-Speed Inlet Stages for an Advanced, High-Pressure-Ratio Core Compressor," NASA TP-1337.

[21] ANSYS CFX-11.0, 2006, ANSYS CFX-Solver Theory Guide, ANSYS Inc.

[22] Chen, H., Huang, X. D., and Fu, S., 2006, "CFD Investigation on Stall Mechanisms and Casing Treatment of a Transonic Compressor," 42nd AIAA/ASME/SAE/ASEE Joint Propulsion Conference & Exhibit, Sacramento, USA, AIAA-2006-4799.

[23] Menter, F. R., 1994, "Two-Equation Eddy-Viscosity Turbulence Models for Engineering Applications," AIAA Journal, Vol. 32, No. 8, pp. 1598-1605.

[24] Kim, J. H., Choi, J. H., and Kim, K. Y., 2010, "Surrogate Modeling for Optimization of a Centrifugal Compressor Impeller," International Journal of Fluid Machinery and Systems, Vol. 3, No. 1, pp. 29-38.

[25] JMP® 6.0.0, 2005, The Statistical Discovery Software, Version 6.0.0, SAS Institute, Inc., Cary, North Carolina, USA.

[26] Sacks, J., Welch, W. J., Mitchell, T. J. and Wynn, H. P., 1989, "Design and Analysis of Computer Experiments," Statistical Science, Vol. 4, No. 4, pp. 409~435.

[27] MATLAB® 7.0, 2004, The Language of Technical Computing, Release 14, The Mathworks Inc., Natick, MA, USA.

[28] Dunham, J., 1998, "CFD Validation for Propulsion System Components," AGARD Advisory Report 355, ISBN 92-836-1075-X.

[29] Giunta, A. A., 1997, "Aircraft Multidisciplinary Design Optimization Using Design of Experimental Theory and Response Surface Modeling Methods," Ph.D. thesis, Department of Aerospace Engineering, Virginia Polytechnic Institute and State University, Blacksburg, VA.

[30] Queipo, N. V., Haftka, R. T., Shyy, W., Goel, T., Vaidyanathan, R., and Tucker, P. K., 2005, "Surrogate-Based Analysis and Optimization," Progress in Aerospace Science, Vol. 41, No. 1, pp. 1-28.

[31] Wilke, I., Kau, H. P., and Brignole, G., 2005, "Numerically Aided Design of a High-Efficient Casing Treatment for a Transonic Compressor," ASME Turbo Expo 2005, Nevada, USA, GT2005-68993.

